Operation and Control of BES-Wind Powered DFIG-Based Microgrid Synchronized to Grid

Sandeep Kumar Sahoo, *Member, IEEE*, Bhim Singh, *Fellow, IEEE*, and Subhadip Chakraborty, *Member, IEEE*

***Abstract*—This article presents operation and control of a grid-interactive wind microgrid (MG) designed for remote areas. MG comprises a doubly fed induction generator (DFIG) and a battery energy storage, operating in both grid-tied and standalone modes. DFIG tied wind turbine functions in maximum power point tracking zone for maximum energy utilization. Based on synchronization/disconnection of DFIG stator to point of common interconnection (PCI) and PCI to the grid, four operating states are identified, managed through solid-state power electronic switches. To address power quality issues under weak distorted grid conditions, this article propose a weight-optimized variable step size adaptive filter-based control for battery-based grid following or grid forming converter. Main novelty of proposed control is its ability to provide enhanced estimation dynamics and stabilize inverter control loops, ensuring superior power quality even during voltage disturbances. Control ensures smooth synchronization and rapid mode transitions using an adaptive enhanced complex coefficient filter-phase locked loop, enabling fast and reliable phase and frequency tracking. MG ensures uninterrupted power supply across all operating states while providing ancillary services, such as harmonic suppression, reactive power injection, and voltage regulation. MATLAB simulations and laboratory validation using a dSPACE DS1202 controller demonstrate that proposed control delivers better dynamic performance and improved power quality compared to conventional approaches.**

***Index Terms*—Adaptive phase locked loop (PLL), battery, doubly fed induction generator (DFIG), grid forming converter, optimized variable weight filter, power quality, synchronization, weak grid.**

I. Introduction

AMID growing energy crisis and environmental challenges, distributed power generation technology has gained significant attention. Key components of this technology include wind turbines, photovoltaic power stations, and energy storage systems. These are interfaced to grid by converters [1], [2]. With pace of rapidly growing energy demand, 8% of worldwide electricity is being harvested from wind [3]. Among various wind generators, doubly fed induction generator (DFIG) is more popular because of reduced converter rating, low price, better efficiency [4], [5]. Battery energy storage (BES) and wind powered DFIG-based microgrid (MG) may be a favorable option for feeding remote prosumers in arctic locations. In remote areas, grid often exhibits erratic behavior, making it challenging for green energy sources to operate independently due to lack of a stable voltage reference. This necessitates use of a grid-forming (GFM) or grid following converter (GFC) (control mode depends on system state and grid availability), which stabilizes voltage and frequency in an MG. In [6], a BES-based GFC is described, where inverter connected to BES ensures regulation of voltage and frequency. In [7], a point of common interconnection (PCI) is established with system using a BES-based GFC. PMSG-based wind energy conversion system (WECS) operates in grid-following (GFL) mode, while BES is utilized to mitigate subsynchronous oscillations. However, this article does not address synchronization control techniques. A reconfigured converter architecture for DFIG, incorporating SMES, is proposed in [8] to enhance fault ride-through performance and GFM capabilities. Dai et al. [9] have proposed a hybrid architecture for conventional GFL PMSG, integrating a GFM-controlled SMES with PMSG. However, SMES systems are costly to construct and maintain, primarily due to high manufacturing expenses of superconducting coils and their maintenance requirements.

Nonlinear or unbalanced loads at PCI often cause unbalanced voltages and currents, adversely affecting power quality. To address this, MG control must mitigate these issues by eliminating harmonics and balancing voltages and currents, thereby protecting sensitive equipment connected to the network. Power quality can be improved using synchronous reference frame (SRF)-based controllers**,** as discussed in [10]. However, in *dq* control, achieving a harmonic-free fundamental component of load currents, requires a tradeoff between steady-state and dynamic performance, influenced by cutoff frequency of low-pass filter [11]. To enhance dynamic performance, several adaptive filtering techniques have been proposed in the literature. In [12], variable sparsity with two least mean square framework-based control is implemented for power quality improvement. However, time complexity of controller is high. In [13], least mean square with an exponential function (LMSEF)-based adaptive control is implemented for grid tied EV charging station supported by solar PV array. An optimized fractional order modified adaptive variable step size LMS control is utilized in [14] for enhancing performance of DVR. In [15], active detection technique-based controller is executed for alleviating power quality issues. However, poor dynamic performances are noticed in these controllers. Model predictive and sliding mode control

Received 29 May 2025; revised 18 October 2025; accepted 8 November 2025. Date of publication 17 November 2025; date of current version 19 January 2026. This work was supported in part by ANRF under Grant RP03357 and Grant RP03195 and in part by UKCERI, SERI-II, FIST Projects. Recommended for publication by Associate Editor M. Molinas. *(Corresponding author: Sandeep Kumar Sahoo.)*

The authors are with the Department of Electrical Engineering, IIT Delhi, New Delhi 110016, India (e-mail: sandeep.kumar.sahoo@ee.iitd.ac.in).

Color versions of one or more figures in this article are available at https://doi.org/10.1109/TPEL.2025.3633199.

Digital Object Identifier 10.1109/TPEL.2025.3633199

(MPSMC)-based shunt active power filter is proposed in [16] for improving non ideal grid power quality. However, combination of MPSMC increments time complexity. Along with that control action is dependent on accuracy of model.

Hence, the focus of this work is development of a distributed MG architecture with a GFM converter. This work also presents a control strategy for a DFIG-based wind energy conversion system that ensures reliable operation during voltage disturbances. This is achieved through advanced PLL-based synchronization and an adaptive weight-optimized filter that enhances power quality and enables accurate estimation. System involves a MG comprising BES system and a wind driven DFIG. BES-based GFC establishes a local grid at PCI. Proposed control framework ensures smooth synchronization (of both stator and grid) and enhances power quality. Key contributions of this article are as follows:

1) Four operating states of DFIG-based MG are identified based on system architecture and PCI's synchronization with grid, with schematics, control, and performance analyzed via simulation and experiments under varying loads and wind conditions.
2) To validate reliable performance of presented control in weak grid situations in simulation and hardware tests. To deploy adaptive enhanced complex coefficient filter-phase locked loop (AECCF-PLL) [18] for fast, stable, and precise frequency and phase-angle estimation, enabling faster synchronization than SRF-PLL under utility restoration, load unbalance, and wind speed variations.
3) To develop a weight-optimized variable step-size adaptive (WOVSSA) filter-based current controller for GFC to extract fundamental components accurately from distorted load currents, with impulsive noise resistance. It is observed to outperform LMSEF [13] and MPSMC [16] counterparts in terms of dynamic and steady-state performance.
4) To present a comparison of computational complexity, settling time, oscillation amplitude, MSD, and % total harmonic distortion (THD) to confirm its effectiveness in overall power quality enhancement.
5) To utilize GFC through control to provide reactive power support, voltage regulation, and harmonic mitigation to improve overall power quality.

Proposed MG is simulated using MATLAB/Simulink and validated through a hardware test bench.

The rest of this article is organized as follows. Section I presents literature review. Section II discusses structure and functioning of MG. Control is presented in Section III. Sections IV presents analyze simulation. Section V describes hardware test results. Finally, Section VI concludes this article.

II. Microgrid Structure and Functioning

Organization of MG is as follows: A wind-driven DFIG-BES-based MG, synchronized with grid, is illustrated in Fig. 1(a). BES establishes local grid at PCI through a GFM converter (GFC), and DFIG is connected to PCI.

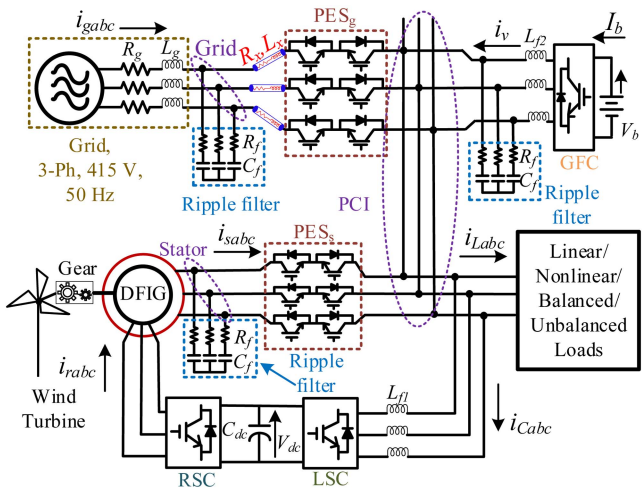

Fig. 1 System architecture∗. ∗Cable (R_x, L_x) and grid Thevenin (R_g, L_g) impedances [values in Appendix].

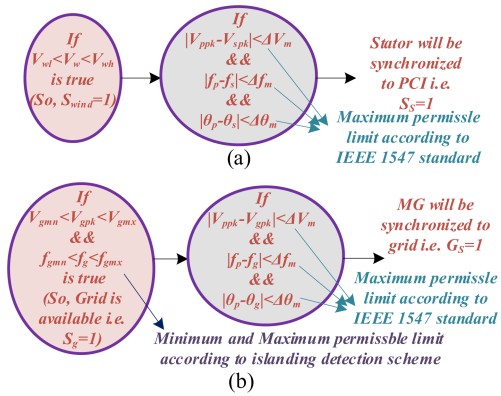

Fig. 2 Generation of (a) stator and (b) grid synchronization signals S_s and G_s.

Wind turbine powers DFIG, which consists of two voltage source converters: load-side converter (LSC) and rotor-side converter (RSC), both linked through a common dc bus. Operational schematic with inter-state mode transition flow diagram is shown in Fig. 2. Stator is synchronized to load PCI via stator static transfer switch (STS), activated by signal S_S. Wind system is synchronized to the grid via grid STS with signal G_S, utilizing both end voltage parameter information and logic checks, as shown in Fig. 2. During high fluctuations in grid voltage beyond threshold, system is disconnected from grid and battery tied inverter operation shifts from grid following to grid forming mode.

In situations when wind speed (V_w) is between cut-in speed (V_{wl}) and cut-out speed (V_{wh}), power can be harnessed from DFIG-based WECS, and status of S_{wind} is activated. RSC establishes voltage across stator terminal. Stator synchronized (SS) status is activated when errors between PCI voltage peak (V_{ppk}) and stator voltage peak (V_{spk}), PCI frequency (f_p) and stator frequency (f_s), and angles of PCI voltage (θ_p) and stator voltage (θ_s) are all within permissible IEEE-1547-2018 [17] range. This connects stator to PCI through a solid-state bidirectional power

TABLE I
MODES OF OPERATION BASED ON SIGNAL STATES

G_S	S_S	State	Remarks	Mode
0	0	S_1	PCI is disconnected from the grid, and stator is disconnected from PCI.	Standalone
0	1	S_2	PCI is disconnected from the grid, and stator is synchronized to PCI.	Standalone
1	0	S_3	PCI is synchronized to the grid, and stator is disconnected from PCI.	Grid
1	1	S_4	PCI is synchronized to grid, and stator is synchronized to PCI	Grid

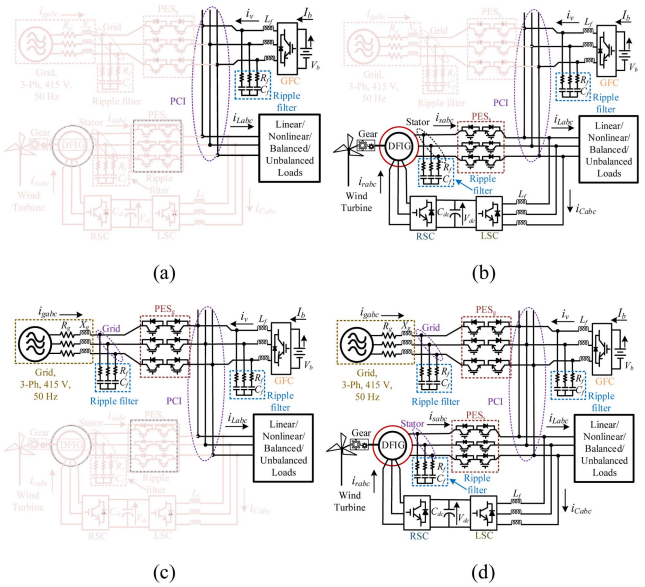

Fig. 3 Different operating states of the microgrid. (a) S_1. (b) S_2. (c) S_3. (d) S_4.

electronics switch (PES_s). Operation schematic is illustrated in Fig. 2(a). Furthermore, islanding detection scheme identifies presence of utility by monitoring utility voltage peak (V_{gpk}) and frequency (f_g) to ensure they remain within permissible limits. Grid synchronized (GS) status is activated when differences between PCI voltage peak (V_{ppk}) and utility voltage peak (V_{gpk}), PCI frequency (f_p) and grid frequency (f_g), and angles of PCI voltage (θ_p) and grid voltage (θ_g) fall within IEEE-1547-2018 [17] specified range. This synchronization connects MG with utility through a solid-state bidirectional power electronics switch (PES_g). Operation schematic is illustrated in Fig. 2(b). For reducing switching ripples in voltage, RC filters are used.

Depending upon synchronization/desynchronization of stator to PCI and synchronization/desynchronization of PCI to grid, four operating states (S_1, S_2, S_3, and S_4) of MG are possible, as given in Table I. States S_1 and S_2 come under standalone mode operation, whereas states S_3 and S_4 come under grid mode operation. Schematic diagram of these operating states is portrayed in Fig. 3(a)–(d).

In state S_1, load demands are catered to by BES-based GFC. In state S_2, wind powered DFIG caters to load demands and surplus wind power charges BES. In State S_3, power from wind generator is unavailable. So, loads are catered to by the utility. Nevertheless, to safeguard utility from detrimental effects caused by nonlinear loads connected at PCI, GFC acts like a distribution static compensator (DSTATCOM). Furthermore, GFC is responsible for power quality improvement of grid. Since grid at remote locations becomes weak due to cabling impedance, GFC helps in voltage regulation at PCI or ensures unity power factor (UPF) operation at grid terminal. BES remains in floating mode. In state S_4, surplus wind power is delivered to grid. Additionally, GFC acts like a DSTATCOM to improve power quality of grid. However, BES stays in idle mode.

III. CONTROL FRAMEWORK

Control architecture of a MG includes management of GFC, RSC, and LSC. This integrated system ensures efficient and seamless operation of MG. Additionally, phase angle estimation technique is portrayed.

A. Frequency and Phase Angle Detection Using AECCF PLL

Accurate estimation of frequency and phase angle is crucial for synchronization and mode transition operations of a MG. In this article, these tasks are addressed using an AECCF-PLL [18]. Grids at remote locations are not ideal because of cabling impedances. So, frequency deviations can arise during synchronization or desynchronization of DFIG stator with PCI, or during connection or disconnection of a MG to main grid, depending on system conditions [19]. This phenomenon is linked to behaviors that arise when forming or disconnecting link between two systems. To achieve seamless synchronization, MG must align its voltage magnitude, frequency, and phase angle with those of grid at PCI. If MG's frequency is not sufficiently matched to grid's frequency prior to synchronization, a sudden frequency correction may occur as MG adjusts to grid. Grid frequency serves as a reference**,** and MG adjusts its frequency to synchronize with grid. However, this process can lead to transient frequency fluctuations if controller is slow. Additionally, sudden changes in load or generation during grid connection can introduce transients, manifesting as frequency deviations. When MG disconnects from grid and enters islanding mode**,** frequency regulation shifts from grid dependence to local generation-demand balance**.** Any mismatch between load and generation during this transition can result in significant frequency deviations as MG's controllers work to stabilize system. Moreover, if synchronization controllers (PLLs) lack sufficient speed or robustness, frequency jumps become more likely. If these frequency deviations persist across multiple mode transitions, they can lead to high transient currents, dynamic oscillations, voltage flicker, protection system tripping, and even load supply failure [20]. SRF-PLL encounters steady state phase error issue when input signal's frequency undergoes a ramp change [18]. However, AECCF PLL handles this issue without hampering stability. Fig. 4 depicts AECCF-PLL, deployed for evaluation of phase angle and frequency. This is an advanced version of ECCF PLL, which incorporates two adaptive complex-coefficient filters to extract positive-negative sequence components, along with an adaptive proportional integral (PI)-based PLL to determine frequency and phase of positive sequence components. To reduce dynamic interactions between voltage-controlled oscillator (VCO) and frequency feedback, VCO input is combined with the integrator output from PI

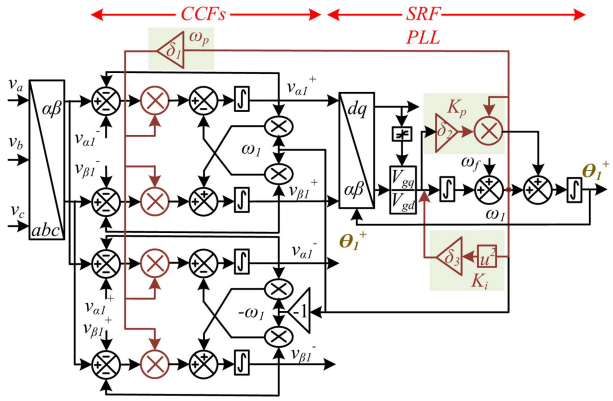

Fig. 4 Structure of AECCF PLL.

controller to estimate frequency. This estimated frequency is used as feedback for filter signal, while an adaptive enhanced PLL structure is utilized to detect parameters of fundamental positive sequence component. Closed loop transfer function is given as

$$CL(s) = \frac{\theta_1{}^+}{\theta_1} = \frac{\omega_p(K_i + K_p s)}{s^3 + (K_p + \omega_p)s^2 + \omega_p K_p s + \omega_p K_i} \quad (1)$$

where as the open loop transfer function is

$$OL(s) = \frac{(K_p + \omega_p)s^2 + \omega_p K_p s + \omega_p K_i}{s^3}. \quad (2)$$

Here, ω_p, K_p, and K_i denote cut off frequency of PLL, proportional and integral gains of PI controller. By combining characteristic polynomial of AECCF-PLL transfer function with unit step response of a third-order system, parameters are obtained as: $\delta_1 = \delta_2 = 0.707$ and $\delta_3 = 0.1215$. In detail analysis can be referred from [18].

B. Control Strategy for Battery Driven GFC

Fig. 5 illustrates GFC control, responsible for following.

1) Establishing a local grid at PCI to maintain terminal voltage and frequency at PCI.
2) Operating in both grid-tied and islanded modes. Providing auxiliary services including reactive power compensation, voltage control, and harmonic filtering in grid tied mode.

GFC control is further explained in two subsections: standalone mode control (SMC) and grid mode control (GMC). States S_1 and S_2 come under SMC whereas, states S_3 and S_4 forces GFC GMC.

1) Standalone Mode Control (SMC): In this mode, direct current control of GFC is utilized, and PCI voltage angle is determined as follows:

$$\theta_p = \int (2\pi f_p *) dt. \quad (3)$$

Here, $f_p{}^*$ (50 Hz) represents reference PCI frequency. Peak value of PCI voltage is calculated as

$$V_{pp}{}^r = (V_{LL}/\sqrt{3}) \times \sqrt{2}. \quad (4)$$

Reference voltages of PCI are acquired as

$$v_{pa}{}^r = V_{pp}{}^r \sin \omega t,\ v_{pb}{}^r = V_{pp}{}^r \sin(\omega t - (2\pi/3))$$
$$v_{pc}{}^r = V_{pp}{}^r \sin(\omega t + (2\pi/3)). \quad (5)$$

Values $V_{pd}{}^*$ and $V_{pq}{}^*$ are derived using *abc*-to-*dq* transformation. Similarly, V_{pd} and V_{pq} are obtained by applying *abc*-to-*dq* transformation to sensed PCI voltages (v_{pabc}). Errors between reference and sensed *dq* voltages are calculated as

$$e_{Vpd} = V_{pd}{}^r - V_{pd},\ e_{Vpq} = V_{pq}{}^r - V_{pq}. \quad (6)$$

Errors are processed using PI controllers for $I_{dq}{}^*$ as

$$I_d{}^* = K_i \int e_{Vpd} dt + K_p e_{Vpd}$$
$$I_q{}^* = K_i \int e_{Vpq} dt + K_p e_{Vpq}. \quad (7)$$

GFC reference currents ($i_{vabc}{}^*$) are obtained through *dq* to *abc* transformation. These reference currents are then compared with sensed currents, and resulting errors are regulated by hysteresis current controllers to generate GFC gating signals.

2) Grid Mode Control (GMC): GFC operates in an indirect current control mode. Taking motivation from [21], in this article, a weight optimized variable step size adaptive (WOVSSA) filter-based current control is proposed and implemented for GMC.

a) Description of WOVSSA filter: WOVSSA filter schematic is portrayed in Fig. 6. WOVSSA filter facilitates active power weight estimation of load currents, enabling UPF operation at grid terminal. In this article, a WOVSSA filter is proposed using least mean fourth (LMF) filter. Equation of weight updation using LMF [22] as

$$G_j(k+1) = G_j(k) + \zeta u_p(k) e(k)^3, \text{ where } j = 0, 1, \ldots . Z-1. \quad (8)$$

Here, ζ is step size, $u_p(k)$ is unit template and $e(k)$ is error function. Four different processes are used for optimization of weights which are: finite impulse response (FIR) filtering, interim estimation of weight, interim estimation of step size and Z-tap adaptive weight updation blocks. Assessment of weight

Optimization is achieved by choosing weight having lower cost function. Let λ represents selection parameter, that establishes relationship between number of filter weights used before and after weight optimization process. Let P be number of optimized weights employed for filtering and Z represents number of weights utilized during optimization, which are correlated as $Z = [P^{\lambda}]$. Where [.] is round off operator. Let $\psi(k)$ be cost function of LMF filter. According to steepest descent algorithm, (8) can be modified as

$$G_j(k+1) = G_j(k) - \zeta[d\psi_j(k)/dG_j(k)]. \quad (9)$$

Rearranging (9), replacing k by k-1 and $d\psi_j(k)/dG_j(k)$ by $\psi_j(k+1) - \psi_j(k)$, equation is updated as

$$\psi_j(k) = \psi_j(k-1) + {}^1/_{\zeta}[G_j(k-1) - G_j(k)]. \quad (10)$$

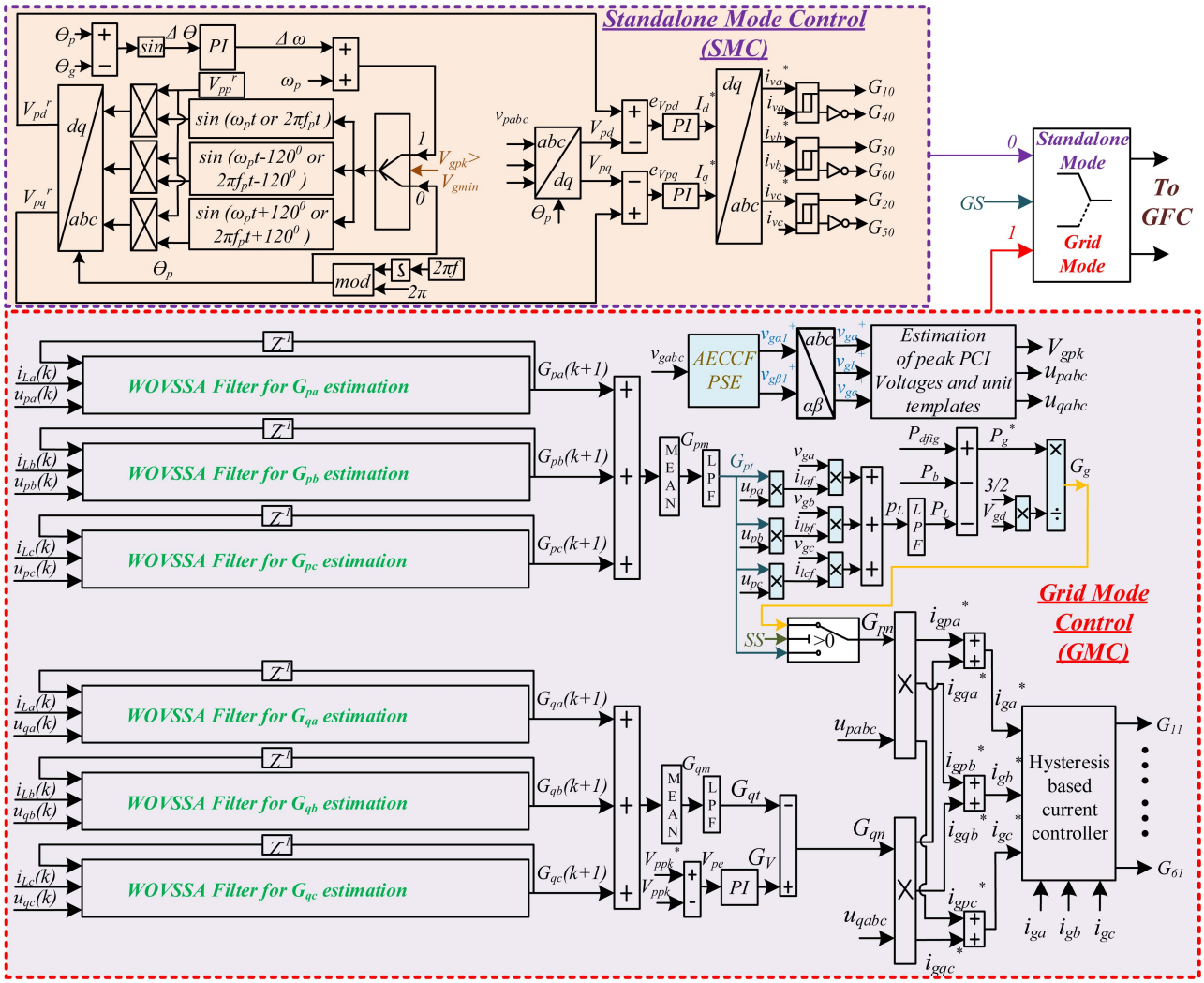

Fig. 5 BES inverter control schematic in standalone and grid-tied modes.

A total of Z minimum cost functions in the weight optimization block can be represented as

$$[\psi_{l,\min}(k)']_{P\times 1} = [\psi_{0,\min}(k)'\,\psi_{0,\min}(k)'\ldots\psi_{P-1,\min}(k)']^T. \tag{11}$$

The variable step size for the adaptive filter can be obtained from (10) as

$$\zeta_j(k) = \frac{G_j(k-1) - G_j(k)}{\psi_j(k) - \psi_j(k-1)}. \tag{12}$$

Therefore, the step size employed for the proposed weight optimization in the WOVSSA filter is expressed as

$$\zeta_{l,j}(k)' = \frac{G_j(k-1) - G_j(k)}{\psi_{l,j}(k) - \psi_{l,j}(k-1)}. \tag{13}$$

In WOVSSA filter, in each iteration step size changes adaptively. Here cost function for weight optimization block is estimated with respect to weights before optimization $G_j(k)$, past optimized weights $G_j(k\text{-}1)'$, past step size $\zeta_{l,j}(k\text{-}1)'$ as

$$\psi_{l,j}(k)' = \psi_{l,j}(k-1)' + {}^{1}/_{\zeta_{l,j}(k-1)'}\,[G_j(k-1)' - G_j(k)']. \tag{14}$$

In the proposed WOVSSA filter, abrupt variations in weights between successive iterations are mitigated through the use of an interim weight estimation block and an interim step-size estimation block, as illustrated in Fig. 6. These interim values are determined based on the minimum cost function.

The interim step size $\mu_{l,j}(k)'$ is estimated using

$$\mu_{l,j}(k)' = \frac{G_j(k-1)' - G_j(k)'}{\rho_{l,j}(k) - \rho_{l,j}(k-1)}. \tag{15}$$

Here, the cost function for the interim step-size evaluation process $\rho_{l,j}(k)$ is computed as

$$\rho_{l,j}(k) = \rho_{l,j}(k-1) + {}^{1}/_{\mu_{l,j}(k-1)'}\,[G_j(k-1)' - C_{l,j}(k)] \tag{16}$$

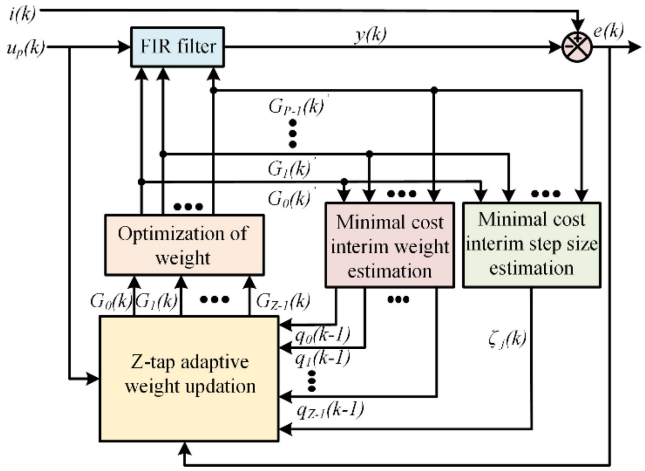

Fig. 6 WOVSSA filter schematic.

where $C_{l,j}(k)$ represents interim estimated weight by using following equation as

$$C_{l,j}(k) = {}^1\!/_2\left[C_{l,j}(k-1) + G_j(k)'\right]. \tag{17}$$

Based on the minimization of a cost function, an interim step size estimation block calculates the optimal step size for the subsequent Z-tap adaptive weight update process as

$$\zeta_j(k) = \arg\min_{\mu_{l,j}(k)'}\{\rho_{\min,j}(k)\}. \tag{18}$$

When the interim estimation finds multiple weights with the same minimal cost, the algorithm uses the average of their step sizes, i.e., $\zeta_j(k)$. For next iteration, minimal cost interim weight is estimated as

$$q_j(k) = \arg\min_{C_{l,j}(k)'}\{\rho_{\min,j}(k)\}. \tag{19}$$

Before optimization, weights are updated as

$$G_j(k+1) = G_j(k) + \zeta_j(k)u_p(k)e(k)^3 + q_j(k). \tag{20}$$

Then by using optimized weights $G_j(k)'$, filtered output of FIR filter is estimated as

$$y(k) = \sum_{l=0}^{P-1} G_l(k)'u_p(k-l) \tag{21}$$

$$e(k) = i(k) - y(k) = i(k) - G(k)'u_p(k)^T. \tag{22}$$

WOVSSA filter algorithm optimization process is given as

b) Estimation of unit templates of grid voltages: From three phase line to line grid voltages (v_{gab}, v_{gbc}), phase voltages are evaluated as

$$v_{ga} = (2v_{gab} + v_{gbc})/3,\ v_{gb} = (-v_{gab} + v_{gbc})/3$$
$$v_{gc} = (-v_{gab} - 2v_{gbc})/3. \tag{23}$$

To overcome adverse effect of grid voltage on current control, these three phase voltages are passed through AECCF-based positive sequence extractor block to obtain two phase positive sequence voltages ($v_{g\alpha\beta 1}{}^+$). Then $\alpha\beta$-*abc* transformation is performed to have three phase filtered voltages ($v_{gabc}{}^+$). Phase

Algorithm

Input: Primary input$i(k)$, reference signal $u_p(k)$
Output: Extracted error$e(k)$
1. Initialize$\zeta_{j,l}(0)'$, Z, P, $G_j(0)$, $G_l(0)'$, $\psi_{l,j}(0)'$
2. $k \leftarrow 1$
3. **While** $k \le N_s$ **do**
4. Calculate cost function of weight optimization block $\psi_{l,j}(k)'$ using (14).
5. Calculate step size that is used for weight optimization $\zeta_{l,j}(k)'$ using (13).
6. Calculate minimal cost function of weight optimization block $\psi_{l,minj}(k)'$ using (11).
7. Find out interim weight $C_{l,j}(k)$ and interim cost function $\rho_{l,j}(k)$ (17) and (16).
8. Calculate interim step size $\mu_{l,j}(k)'$ by using (15).
9. Estimate the minimal cost interim step-size $\zeta_j(k)$ and interim weight $q_j(k)$ using (18) and (19) respectively.
10. On basis of optimized weight $G_j(k)'$ using (21) to get $y(k)$.
11. By using (22), error signal is obtained.
12. Z weights are to be updated prior optimization using equation: $G_j(k+1) = \zeta_j(k)u_p(k)e(k)^3 + q_j(k)$.
13. $k \leftarrow k+1$

end while.

peak of grid voltages (V_{gpk}) is given as

$$V_{gpk} = \sqrt{0.67 \times \left((v_{ga}{}^+)^2 + (v_{gb}{}^+)^2 + (v_{gc}{}^+)^2\right)}. \tag{24}$$

In phase unit templates of grid voltages are obtained as

$$u_{pa} = v_{ga}{}^+/V_{gpk},\ u_{pb} = v_{gb}{}^+/V_{gpk},\ u_{pc} = v_{gc}{}^+/V_{gpk}. \tag{25}$$

The quadrature unit templates of grid voltages are estimated as

$$u_{qa} = \frac{-u_{pb} + u_{pc}}{\sqrt{3}},\ u_{qb} = \frac{\sqrt{3}u_{pa}}{2} + \frac{u_{pb} - u_{pc}}{2\sqrt{3}}$$
$$u_{qc} = -\frac{\sqrt{3}u_{pa}}{2} + \frac{u_{pb} - u_{pc}}{2\sqrt{3}}. \tag{26}$$

c) Estimation of fundamental active load current weight: Using WOVSSA algorithm, from load currents (i_{Labc}) fundamental active and reactive components of load currents are separated. This adaptive variable step size algorithm ensures accurate and fast estimation of weights of load currents during steady state and dynamic conditions. For phase "*a*" load current, estimation of fundamental active component is performed as

$$G_{pa}(k+1) = G_{pa}(k) + \zeta(k)u_{pa}(k)e_{la}(k)^3 \tag{27}$$

where the error is as

$$e_{pa}(k) = i_{La}(k) - G_{pa}(k-1)u_{pa}(k). \tag{28}$$

Similarly, active power weights of phase "b" and phase "c" load currents (G_{pb}, G_{pc}) are extricated using WOVSSA filter by using (27). Mean of active power weights are estimated as

$$G_{pm} = (G_{pa} + G_{pb} + G_{pc})/3. \tag{29}$$

Thereafter, a low pass filter (LPF) filters G_{pm}, which gives net active weight component of load currents i.e., G_{pt}.

Likewise, for phase "*a*" of load current, estimation of fundamental reactive component is performed as

$$G_{qa}(k+1) = G_{qa}(k) + \zeta(k) u_{qa}(k) e_{qa}(k)^3 \tag{30}$$

where error is as

$$e_{qa}(k) = i_{La}(k) - G_{qa}(k-1) u_{qa}(k). \tag{31}$$

Similarly, reactive power weights of phase "*b*" and phase "*c*" load currents (G_{qb}, G_{qc}) are extricated using WOVSSA filter by using (30). Mean of active power weights are given as

$$G_{qm} = (G_{qa} + G_{qb} + G_{qc})/3. \tag{32}$$

Thereafter, an LPF filters G_{qm}, which gives the net reactive weight component of load currents, i.e., G_{qt}.

d) Estimation of reference active grid current components: Depending upon availability of wind power generation i.e., $S_S = 0$ or 1, the net active weight component of grid current (G_{pn}) is estimated as

$$G_{pn} = \begin{Bmatrix} G_{pt}, \text{when } S_s = 0 \\ G_g, \text{when } S_s = 1 \end{Bmatrix}. \tag{33}$$

When, $S_S = 0$, i.e., wind power is unavailable, at that time load demand is fulfilled by utility. When $S_S = 1$, surplus power of MG is delivered to grid. G_g is estimated as follows. Net active weight component of load currents i.e., (G_{pt}) is multiplied with unit templates of grid voltages (u_{pabc}) to obtain fundamental component nonlinear load currents (i_{labcf}) as follows:

$$i_{laf} = G_{pt} * u_{pa}, i_{lbf} = G_{pt} * u_{pb}, i_{lcf} = G_{pt} * u_{pc}. \tag{34}$$

Fundamental instantaneous load active power is derived as

$$p_L = v_{ga} * i_{laf} + v_{gb} * i_{lbf} + v_{gc} * i_{lcf}. \tag{35}$$

Then fundamental load active power (P_L) is estimated from p_L by processing it through a LPF of cut off frequency 100 Hz. Surplus MG power is reference grid power, estimated as

$$P_g* = P_{dfig} - P_b - P_L \tag{36}$$

where P_{dfig} and P_b are power generated from wind driven DFIG unit and BES power, respectively. G_g is evaluated as

$$G_g = P_g/(3 * V_{gd}/2) \tag{37}$$

where V_{gd} is *d*-axis component of grid voltage. Reference active components of grid currents are evaluated by product of grid voltage in phase unit templates and net active weight as

$$i_{gpa}* = u_{pa} \times G_{pn},\ i_{gpb}* = u_{pb} \times G_{pn},\ i_{gpc}* = u_{pc} \times G_{pn}. \tag{38}$$

e) Estimation of reference grid reactive currents: An error between reference and actual peak values of PCI voltage is expressed as

$$V_{pe} = V_{ppk} * -V_{ppk}. \tag{39}$$

A PI voltage regulator is used with this error to maintain PCI voltage by producing reactive loss component G_v as follows:

$$G_v = K_{pv} V_{pe} + K_{ir} \int V_{iv} dt. \tag{40}$$

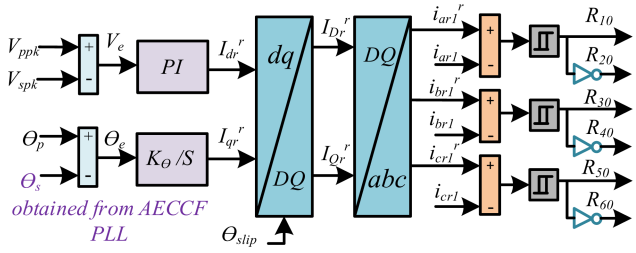

Fig. 7 RSC control prestator synchronization.

Net reactive weight component of load currents is subtracted from reactive loss component to produce net reactive weight component of grid current (G_{qn}) as follows:

$$G_{qn} = G_v - G_{qt}. \tag{41}$$

Moreover, for UPF at grid, G_{qn} is taken as zero. Reference reactive components of grid currents are evaluated by product of grid voltage quadrature unit templates and net reactive weight of grid currents as follows:

$$i_{gqa}* = u_{qa} \times G_{qn},\ i_{gqb}* = u_{qb} \times G_{qn},\ i_{gqc}* = u_{qc} \times G_{qn}. \tag{42}$$

f) Generation of switching pulses for GFC: Adding respective active ($i_{gpabc}{}^*$) and reactive components of grid currents ($i_{gqabc}{}^*$), three phase reference grid currents ($i_{gabc}{}^*$) are produced. Then acquired grid reference currents ($i_{gabc}{}^*$) and sensed grid currents (i_{gabc}) are compared, and errors are controlled by hysteresis current controllers for generating gate pulses for GFC in GCM.

C. Control Strategy for LSC

In this article, a VOC-based LSC strategy is implemented. Control tasks assigned to LSC include: maintaining the interlinking dc-bus voltage.

Detailed information about LSC control technique implemented in this work can be found in [23].

D. Control Strategy for RSC

RSC controller is responsible for the following tasks.

1) *Control Before Stator Synchronization:* It establishes and maintains voltage and phase across stator terminals.
2) *Control After Stator Synchronization:* It delivers reactive power support to ensure the stator operates at UPF while maximizing power extraction from WECS.

1) RSC Control Prestator Synchronization (i.e., When $S_S = 0$*):* Fig. 7 illustrates the RSC control process prior to stator synchronization. Voltage buildup process at stator terminal is initiated when status of S_{wind} becomes active. (27) demonstrates estimation of peak value of grid voltage (V_{gpk}). Similarly, peak value of stator voltages (V_{spk}) is also estimated.

Error among peak of PCI and stator voltage is given as

$$V_e = V_{pp} - V_{sp}. \tag{43}$$

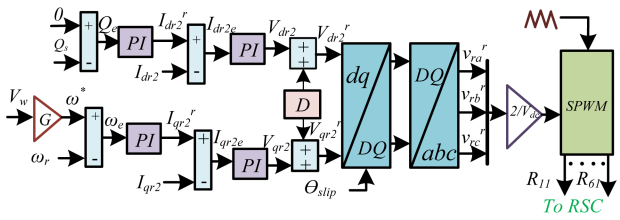

Fig. 8. RSC control post-stator synchronization.

V_e is then passed through a PI controller to derive ${I_{dr}}^r$, as

$$ {I_{dr}}^r = K_{pr} V_e + K_{ir} \int V_e dt. \tag{44}$$

Error between the angles of PCI voltages and stator voltages is expressed as

$$\theta_e = \theta_p - \theta_s. \tag{45}$$

This error is regulated by an integral controller to obtain ${I_{qr}}^r$ as follows:

$$ {I_{qr}}^r = K_\theta \int \theta_e dt. \tag{46}$$

To obtain ${I_{rD}}^*$ and ${I_{rQ}}^*$, dq transformation is done as follows:

$$\begin{aligned} {I_{Dr}}^r &= {I_{dr}}^r \cos(\theta_{\text{slip}}) - {I_{qr}}^r \sin(\theta_{\text{slip}}) \\ {I_{Qr}}^r &= {I_{dr}}^r \sin(\theta_{\text{slip}}) + {I_{qr}}^r \cos(\theta_{\text{slip}}). \end{aligned} \tag{47}$$

Reference RSC currents are obtained as

$$\begin{aligned} {i_{ar1}}^r &= {I_{Dr}}^r,\ {i_{br1}}^r = -1/2 {I_{Dr}}^r + \sqrt{3}/2 {I_{Qr}}^r \\ {i_{cr1}}^r &= -1/2 {I_{Dr}}^r - \sqrt{3}/2 {I_{Qr}}^r. \end{aligned} \tag{48}$$

Hysteresis controllers manage errors between sensed and reference RSC currents to generate switching signals for RSC.

2). RSC Control Poststator Synchronization (i.e., When $S_S = 1$*):* Fig. 8 shows RSC control after stator synchronization. As synchronization is achieved, control mode transitions to power control. Reactive power demand of DFIG is fulfilled by RSC, resulting in a stator reference reactive power of zero. Error between reference and actual stator reactive power is given as

$$Q_e = -Q_s. \tag{49}$$

PI controller is used with error to generate ${I_{rd2}}^*$ as follows:

$$ {I_{dr2}}^r = K_{pr2} Q_e + K_{ir2} \int Q_e dt. \tag{50}$$

Optimum tip speed ratio-based maximum power point tracking algorithm is used to determine reference rotor speed for maximizing power extraction. Error between reference and measured rotor speed is given as

$$\omega_e = \omega * - \omega. \tag{51}$$

PI controller is used with error to generate ${I_{rq2}}^*$ as follows:

$$ {I_{qr2}}^r = K_{pr4} \omega_e + K_{ir4} \int \omega_e dt. \tag{52}$$

${I_{dr2}}^r$ is compared with I_{dr2}, and resulting error is as

$$ I_{dr2e} = {I_{dr2}}^r - I_{dr2}. \tag{53}$$

${I_{qr2}}^r$ is compared with I_{qr2}, and resulting error is as

$$ I_{qr2e} = {I_{qr2}}^r - I_{qr2}. \tag{54}$$

These errors are fed to two PI controllers as follows:

$$\begin{aligned} V_{dr2} &= K_{pr5} I_{dr2e} + K_{ir5} \int I_{dr2e} dt \\ V_{qr2} &= K_{pr5} I_{qr2e} + K_{ir5} \int I_{qr2e} dt. \end{aligned} \tag{55}$$

V_{dr2} and V_{qr2} are then combined with decoupling term "D" to derive ${V_{dr2}}^r$ and ${V_{qr2}}^r$, respectively. Subsequently, *dq-DQ* and *DQ-abc* transformations are performed to generate three-phase rotor reference voltages (${v_{rabc}}^r$). These voltages are scaled by a factor of $2/V_{\text{dc}}$ to implement SPWM control, which ultimately generates gate pulses for RSC.

IV. Analysis of Simulation Results

System is modeled and simulated in MATLAB/Simulink 2017b, incorporating nonlinear loads. In State S_4, performance is evaluated under dynamic load variations, and extreme wind speed fluctuations representing severe weather conditions. Parameters and system ratings are given in Appendix.

A. Performance Study During Dynamic Load Variations

Fig. 9(a) portrays performance during dynamic load variations. At 3.4 s, load changes from nonlinear load to combination of linear and nonlinear loads. Power delivered to load (P_L) increases as magnitude of load current (i_L) increases. As power demand of load increases, the power delivered to grid decreases, which is confirmed from decreased grid current (i_g). Because of proper harmonics and reactive power compensation by battery converter, grid operates at UPF. As GFC acts as a DSTATCOM (whose current is "i_v"), i_g becomes sinusoidal irrespective of presence of nonlinear/combined linear and nonlinear loads at PCI. In grid connected mode, BES remains in floating mode as displayed in Fig. 9(a), which is confirmed from BES current (I_b).

B. Performance Study During Dynamic Wind Variations

Performance during extreme weather condition, which affect wind generation is portrayed in Fig. 9(b). In state 'S_4' at 3.55 s wind speed (V_w) changes from 6 to 11.55 m/s. Accordingly, because of peak power point tracking operation, rotor speed is changing from 102 to 195.5 rad/s. Tip speed ratio (TSR = λ) is maintained at its optimal value (i.e., 8.1 m/s), which ensures peak power point tracking operation of WECS. With changes in wind speed, stator current (i_s) is changing accordingly. Increasing wind power delivers more power to grid, as confirmed by grid current (i_g). Load current (i_L) remains unperturbed during wind speed transition. GFC provides harmonic and reactive power compensation for maintaining terminal voltage, which is confirmed by GFC current "i_v." In grid-connected mode, BES remains in floating mode as displayed in Fig. 9(b), which is confirmed from I_b.

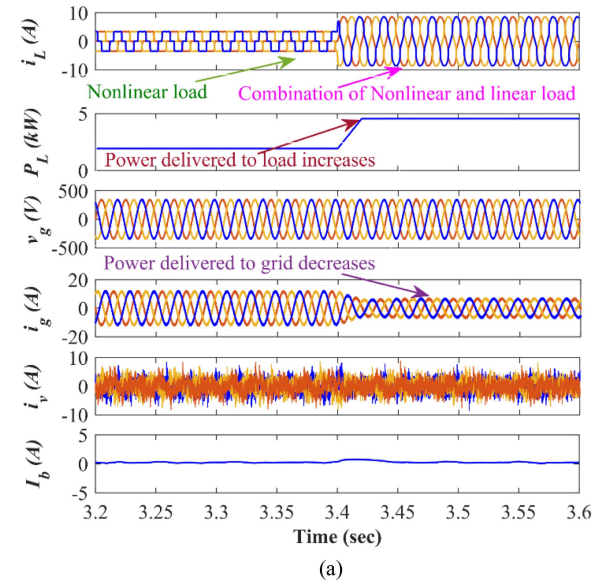

(a)

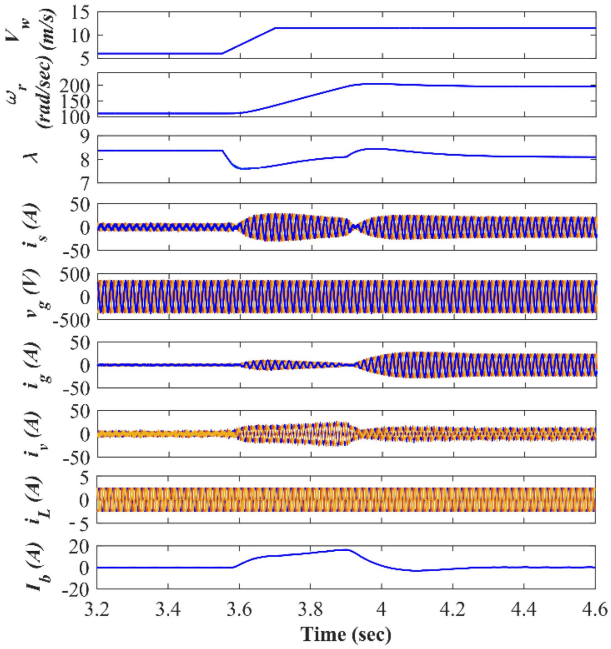

(b)

Fig. 9 (a) Performance during dynamic load variations. (b) Performance during extreme wind speed change.

Fig. 10 Hardware setup of distributed wind microgrid with battery.

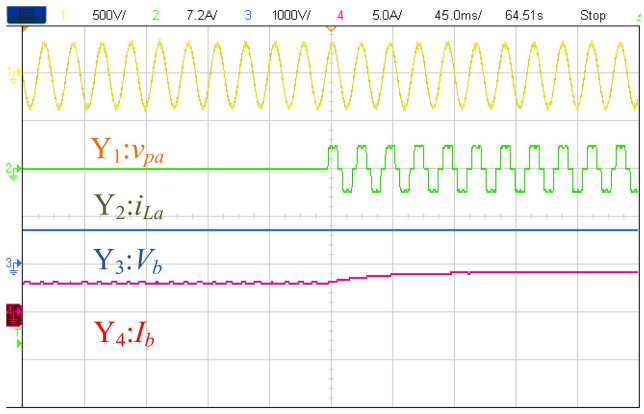

(a)

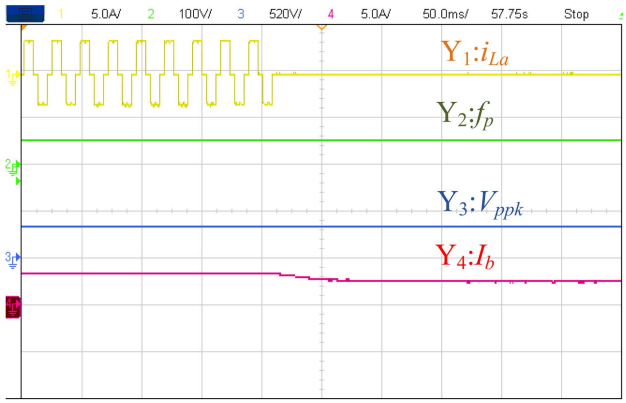

(b)

Fig. 11. MG performance in stateS_1during load unbalancing.(a)v_{pa}= 500 V/div, i_{La}= 7.2 A/div, V_b= 1000 V/div, I_b= 5 A/div.(b)i_{La}= 5 A/div, f_p= 100 V/div, V_{ppk}= 520 V/div, I_b= 5 A/div.

V. Analysis of Test Results

This system is implemented on a custom-developed hardware rig, and its performance is evaluated. A DFIG with a rating of 11 kW, 415 V, and 50 Hz is mechanically coupled to a squirrel cage induction motor (SCIM). SCIM is controlled to emulate characteristics of a three-blade wind turbine. Control architecture is realized using a dSPACE MicroLabBox (DS1202). Performance metrics are recorded using specialized instruments: steady-state results are measured with a six-channel HIOKI power quality analyzer, while dynamic responses are captured using Keysight and Tektronix four-channel digital storage oscilloscope. Additionally, stator of DFIG is synchronized to point of common intersection (PCI) through two solid-state switches, facilitating delivery of generated wind power to PCI. Fig. 10 shows hardware setup.

A. Performance Study in Different Operating States

Performances of system are discussed in detail in each operating state. Performance of MG in state S_1 is presented in Fig. 11. When load is attached to phase "*a*," BES shifts from charging to discharging mode which is observed from BES current (I_b) as shown in Fig. 11(a). BES voltage (V_b) is maintained. During

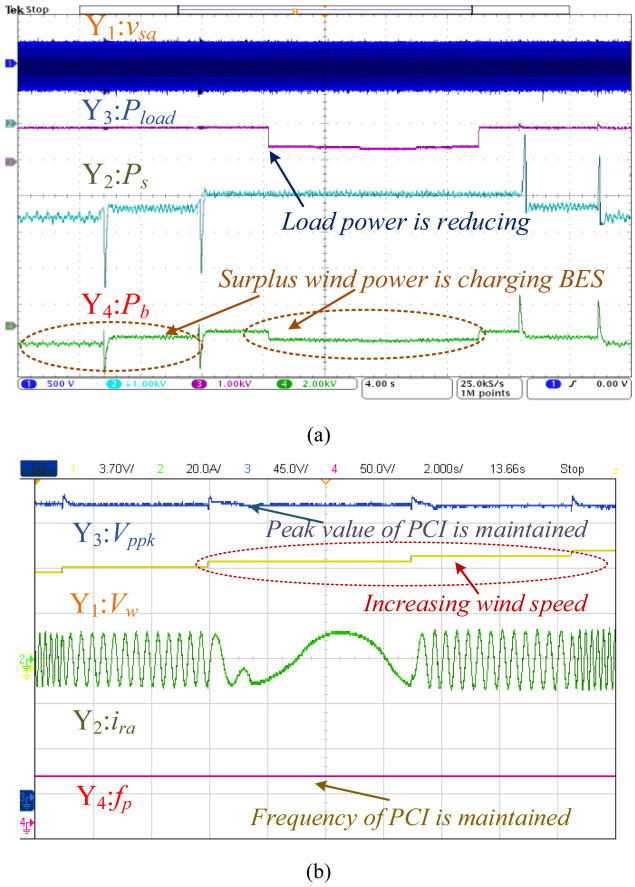

Fig. 12 MG performance in stateS_2 during load/wind change. (a)v_{sa}= 500 V/div, P_s= 1 kV/div, P_{load} = 1 kV/div, P_b= 2 kV/div. (b)V_w= 3.7 V/div, i_{ra}= 20 A/div, V_{ppk}= 45 V/div, f_p= 50 V/div.

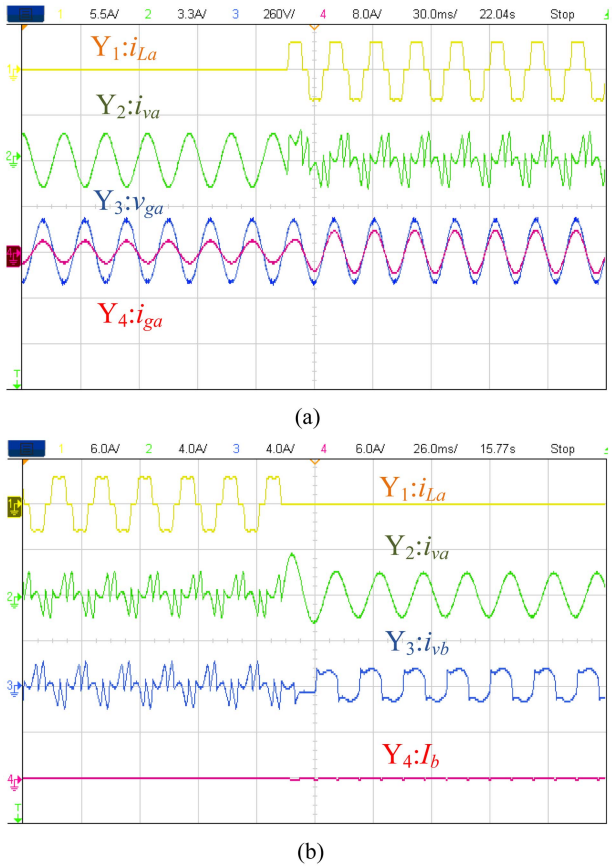

Fig. 13. MG performance in state S_3 during load unbalancing. (a)i_{La}= 5.5 A/div, i_{va}= 3.3 A/div,v_{ga}= 260 V/div, i_{ga}= 8 A/div. (b)i_{La}= 6 A/div, i_{va}= 4 A/div, i_{vb}= 4 A/div, I_b= 6 A/div.

load unbalancing from phase "*a*," regulated frequency (f_p) and peak of PCI voltage (V_{ppk}) are shown in Fig. 11(b).

Fig. 12(a) and (b) illustrates performance of MG during load/wind change in state S_2. In this mode, after fulfilling load demand surplus wind power is stored in BES, which is portrayed in Fig. 12(a). In Fig. 12(b), during wide variation of wind speed, peak value of PCI voltage and frequency remain regulated.

Performance of MG during load unbalancing in state S_3 is presented in Fig. 13. In this state, power from wind generator is not available. So, load demand is fulfilled by grid. GFC acts like a DSTATCOM. When nonlinear load is attached to phase "*a*," harmonic compensation is provided by GFC, which is viewed from GFC current "i_{va}." Grid voltage and current are in phase, which notifies UPF operation of grid. Load demand is fulfilled by utility. These are demonstrated in Fig. 13(a). When load is removed from phase "*a*," no compensation is provided by phase "*a*" of GFC whereas, compensation is provided by other phases. These can be viewed from GFC currents "i_{va}" and "i_{vb}" in Fig. 13(b). In grid tied mode operation BES remains floating, as seen from BES current (I_b).

Fig. 14(a)–(f) illustrates performance of MG during load/wind change in state S_4. Fig. 14(a)–(b) portray performance during voltage regulation. In Fig. 14(a), when load is attached to phase "*a*," compensation is provided by GFC as indicated from "i_{va}." "v_{ga}" and "i_{ga}" are shown, which convey power is delivered to grid and voltage regulation is ensured. Real power delivered to grid (P_g) and reactive power delivered by GFC (Q_{gfc}) are demonstrated in Fig. 14(b). With increase in nonlinear load, 'P_g' decreases. During load unbalancing more reactive power support is provided by GFC to sustain the PCI voltage. When load becomes balanced, "Q_{gfc}" decreases. Fig. 14(c)-(e) showcase performance during UPF operation. When nonlinear load is connected to phase "*a*," harmonic compensation is provided by GFC as confirmed from "i_{va}" which is showcased in Fig. 14(c). "v_{ga}" and "i_{ga}" are out of phase which confirm power is delivered to grid at UPF. With load attached to PCI in phase "*a*," "P_g" decreases. However, "Q_g" is maintained at zero ensuring UPF operation. These are shown in Fig. 14(d). Fig. 14(e) shows "I_b," which signifies BES floats in grid mode. Additionally, "i_{va}" and "i_{vb}" are shown during load unbalancing in UPF operation. Fig. 14(f) showcases performance during wind speed variation. In grid tied mode, with increase in wind speed more power is delivered to the grid, which is visualized in Fig. 14(f).

B. Synchronization/Desynchronization Performance of Stator

Seamless connection and disconnection of stator are illustrated in Fig. 15(a) and (b). Stator's connection performance is detailed in Fig. 15(a). When wind speed exceeds minimum threshold V_{wl}, voltages are induced at stator terminals, gradually

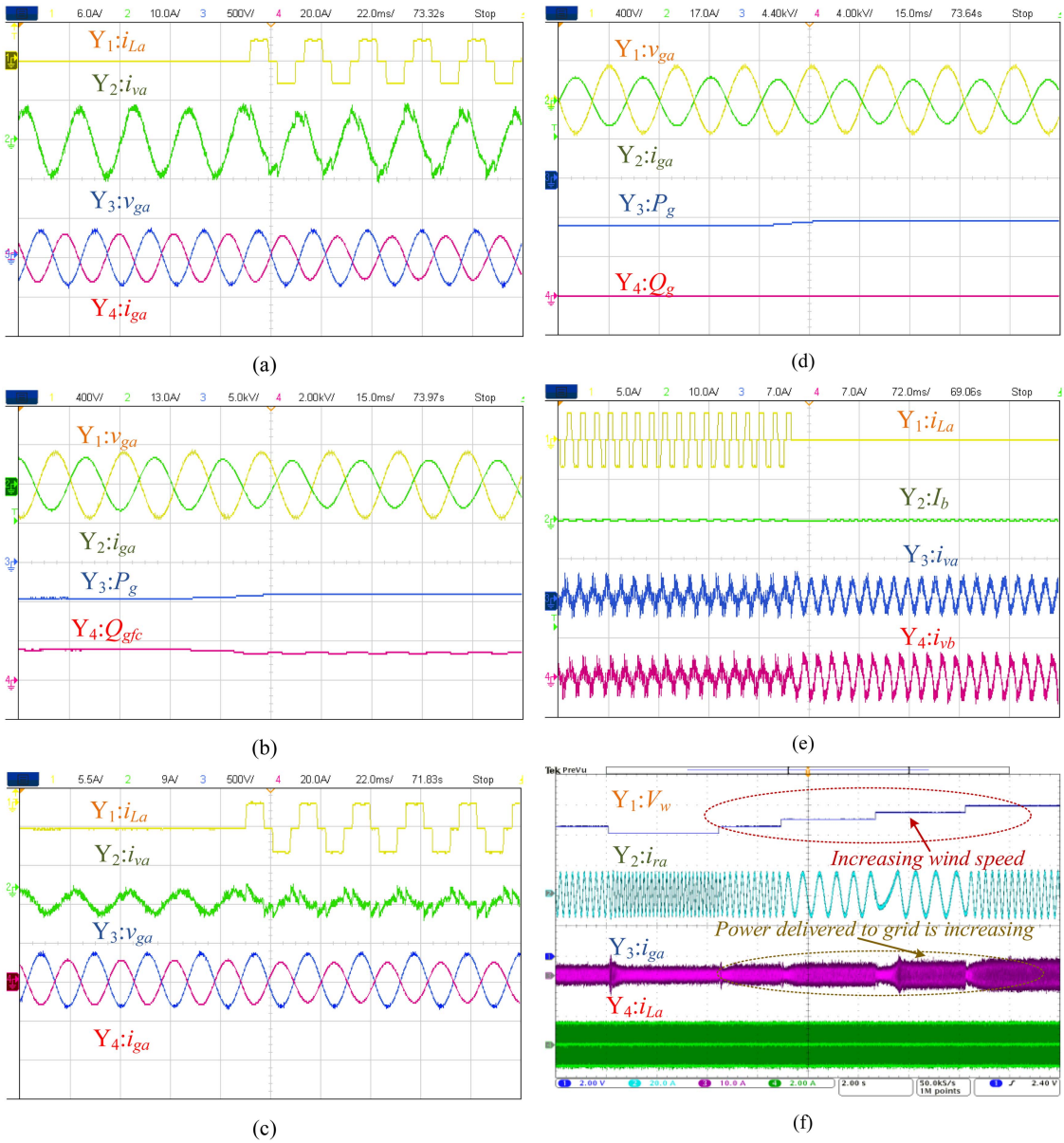

Fig. 14 MG performance in S_4during load change in voltage regulation operation. (a)i_{La}= 6 A/div, i_{va}= 10 A/div, v_{ga}= 500 V/div, i_{ga}= 20 A/div. (b)v_{ga}= 400 V/div, i_{ga}= 13 A/div, P_g= 5 kW/div, Q_{gfc}= 2 kVAR/div. During load change in UPF operation. (c) i_{La}= 5.5 A/div, i_{va}= 9 A/div, v_{ga}= 500 V/div, i_{ga}= 20 A/div. (d)v_{ga}= 400 V/div, i_{ga}= 17 A/div, P_g= 4.4 kW/div, Q_g= 4 kVAR/div. (e)i_{La}= 5 A/div, I_b= 10 A/div, i_{va}= 7 A/div, i_{vb}= 7 A/div. (f) performance during wind change. (f)V_w= 2 V/div,i_{ra}= 20 A/div, i_{ga}= 10 A/div, i_{La}= 2 A/div.

aligning with PCI voltages generated by BES-GFC. Once voltage falls within the specified limits of IEEE-1547-2018, stator connects to PCI, indicated by $S_S = 1$. Subsequently, stator begins delivering power to PCI. Seamless disconnection of stator is illustrated in Fig. 15(b). When wind speed drops below V_{wl}, stator is disconnected, indicated by $S_S = 0$. Synchronization is executed by control within six cycles (120 ms), which is within the 10-cycle standard as per the IEEE std. 1547 [17].

C. Synchronization/Desynchronization Performance of Grid

Seamless connection and disconnection of grid are illustrated in Fig. 16(a) and (b). Grid connection performance is detailed in Fig. 16(a). Upon availability of grid, angle of grid voltage appears. Because of appropriate controller action angle of PCI voltage tries to align with that of grid. Once error tolerance falls within specified limits of IEEE-1547-2018 [17], MG is connected to grid, which is indicated by $G_S = 1$. Subsequently, grid current starts flowing. Seamless disconnection of grid is illustrated in Fig. 16(b). When grid is unavailable, grid is disconnected, indicated by $G_S = 0$. At this point, grid voltage ceases, while PCI voltage is sustained, as shown in Fig. 16(b). Load current i_{La} remains unperturbed.

D. Assessment of Power Quality

Assessment of power quality is rendered in Fig. 17(a) and (b). Voltages at stator (v_{sabc}), stator currents (i_{sabc}), voltages at

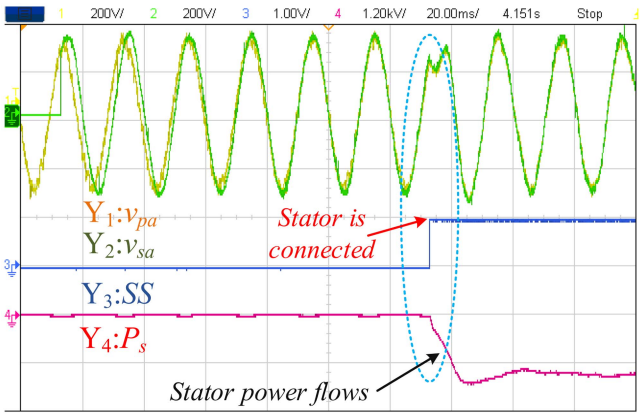

(a)

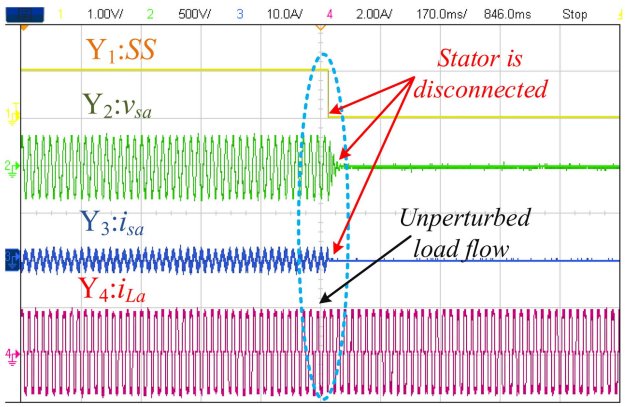

(b)

Fig. 15 Performance during stator connection/disconnection (a) v_{pa}, v_{sa}= 200 V/div, S_S= 1 V/div, P_s= 1.2 kW/div(b) S_S = 1 V/div, v_{sa} = 500 V/div, i_{sa} = 10 A/div, i_{La} = 2 A/div. voltage and current cease, while load currents remain uninterrupted, as shown in (b).

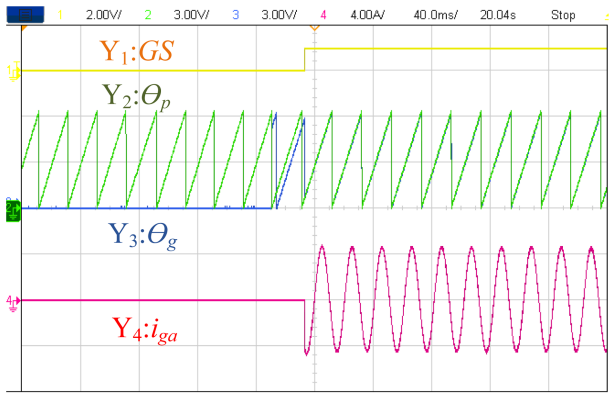

(a)

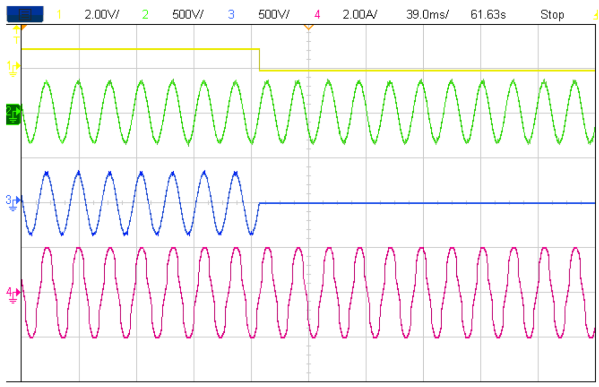

(b)

Fig. 16 Performance during grid connection/disconnection. (a) G_S= 2 V/div, θ_p= 3 V/div, θ_g= 3 V/div, i_{ga}= 4 A/div. (b) G_S= 2 V/div, v_{pa}= 500 V/div, v_{ga}= 500 V/div, i_{La}= 2 A/div.

PCI (v_{pabc}) and load currents (i_{Labc}) are depicted in Fig. 17(a). Because of proper control of RSC, stator operates at UPF. Despite of presence of highly nonlinear load at PCI, THDs of stator voltage and stator current are maintained 4.254% and 3.116%, respectively. Grid voltages (v_{gabc}), grid currents (i_{gabc}), PCI voltages (v_{pabc}) and load currents (i_{Labc}) are portrayed in Fig. 17(b). Despite of presence of highly nonlinear loads (of THD 29.966%), grid voltage THD is maintained at 6.395% and grid current THD is maintained at 3.161% which are abided by IEEE-1547-2018 std [17]. Power is delivered at UPF to PCI. The grid voltage is kept distorted as part of a weak grid-tied degraded grid voltage quality test case to validate reliable performance of proposed control under voltage distortion conditions. This allows analysis of control's steady-state behavior, demonstrating that grid currents remain within a 5% THD limit [17], despite distorted grid voltages. Distortions at the incoming feeder can arise from the distributed nature of the power system and the presence of nonlinear loads in distributed upstream feeders [test case Fig. 17(b) emulates such distorted voltage grid-tied mode situations].

E. Comparison of Performances of AECCF PLL and SRF PLL

To evaluate performance of PLL, a simulation study is conducted in Simulink/MATLAB-2017b. Performance characteristics are illustrated in Fig. 18. At 3.55 s, utility is restored, load unbalancing occurs, and wind speed changes simultaneously. Resulting frequency variations are observed for both SRF PLL and AECCF PLL [18], as depicted in Fig. 18. The analysis reveals a significant frequency dip in the SRF PLL's estimation, whereas AECCF PLL exhibits a much smaller dip. Additionally, phase angle estimation of grid voltages under these conditions-utility restoration, load unbalance, and wind speed variation are compared between SRF PLL and AECCF PLL. These results show that SRF PLL introduces a phase difference between grid voltage and PCI voltage, whereas AECCF PLL maintains better accuracy. Due to its faster and precise voltage phase angle estimation, AECCF PLL ensures faster synchronization than SRF PLL.

F. Performance Comparison of Different Controllers

Table II presents computational complexity and performance comparison of various controllers, highlighting superiority of proposed WOVSSA filter-based MG control over existing state-of-the-art techniques. For filter length of "N," computational complexity of proposed WOVSSA filter, least mean square with

TABLE II
PERFORMANCE COMPARISON OF VARIOUS CONTROLS

Features		Control Algorithms		
		LMSEF [13]	MPSMC [16]	WOVSSA (Proposed)
Computational Complexity	×	$2N+1$	$3N+3$	$2N+1$
	+	$2N$	$3N+1$	$2N$
	÷	0	0	3
	Sign(.)	N	0	0
	Exp(.)	N	0	0
Cost Function		$[e(k)]^2$	$\sum_{c=1}^{N}[(\dot{y}(k+c\|m)-r(k+c))^T \times Q(k+c)(\dot{y}(k+c\|m)-r(k+c)]$	$[e(k)]^4$
%Peak Overshoot (%M_p)		0.512	0.731	0.415
2% Settling Time (ms)		142 ms	166 ms	55 ms
Oscillation Amplitude in Steady State (Peak to Peak in A)		0.18 A	0.13 A	0.035 A
MSD (dB)		-58 dB	-62 dB	-76 dB
THD (%) grid current		3.81%	3.21%	1.41%

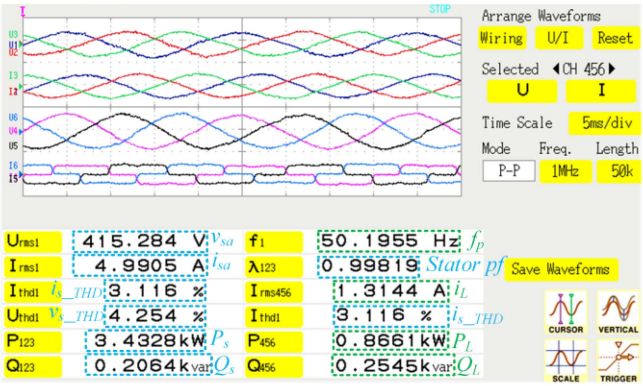

(a)

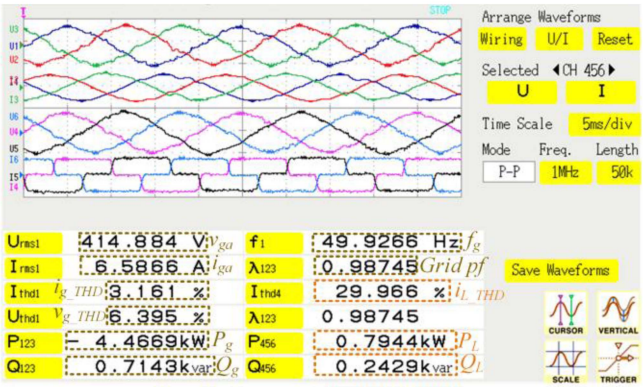

(b)

Fig. 17 Power quality assessment. (a) in standalone mode: ChV_{123}: v_{sabc}= 750 V/div, ChI_{123}: i_{sabc}= 15 A/div, ChV_{456}: v_{pabc}= 750 V/div, ChI_{456}: i_{Labc}= 4 A/div. (b) in weak grid connected mode with distorted voltage test case: ChV_{123}: v_{gabc}= 750 V/div, ChI_{123}: i_{gabc}= 15 A/div, ChV_{456}: v_{pabc}= 750 V/div, ChI_{456}: i_{Labc}= 2 A/div.

an exponential function (LMSEF) filter [13] and MPSMC [16] filter is $4N+4$, $6N+1$, and $6N+4$, respectively. This signifies least computational complexity of proposed controller. Settling time of proposed controller is least as compared to that of other controllers. Along with that, peak to peak oscillation amplitude

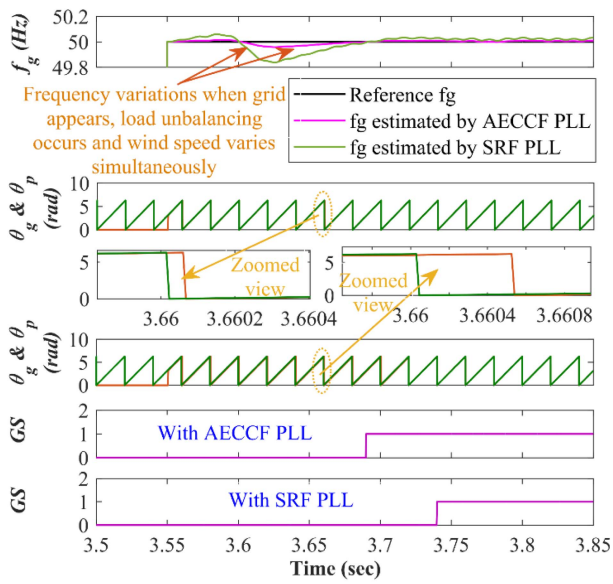

Fig. 18 Comparison of frequency, angle of grid voltages and synchronization performance obtained by AECCF-PLL and SRF-PLL.

in steady state is least in case of WOVSSA filter control. During load unbalancing, comparative assessment of WOVSSA control algorithm with contemporary control methods like LMSEF [13], MPSMC [16], is demonstrated in Fig. 19. To have this comparison, load unbalanced is done in one phase "a" at 1s and corresponding weights of different controllers are plotted. It can be concluded that, proposed control has quicker response than its counterparts as weight becomes zero early. Settling time of proposed controller is least as compared to that of other controllers. Along with that, peak to peak oscillation amplitude in steady state is least in case of WOVSSA filter control.

Fig. 20 depicts mean square deviations plots of different control algorithms, which conveys least MSD of the proposed controller. Fig. 21 portrays power quality evaluation for various controllers from which it can be confirmed that least THD is obtained for proposed controller.

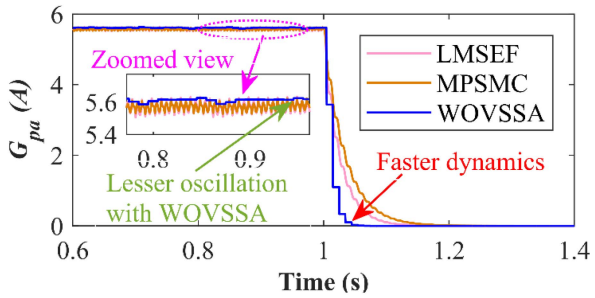

Fig. 19 Comparative assessment of WOVSSA control with contemporary controls during load unbalancing.

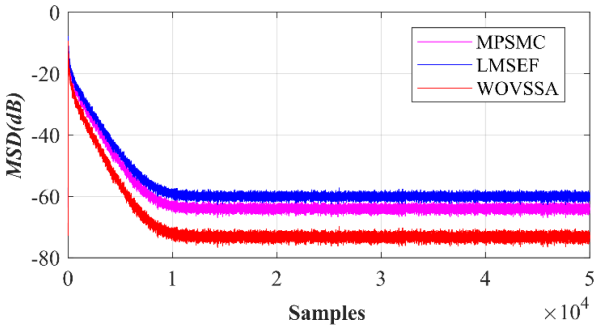

Fig. 20 MSD plots of different control algorithms.

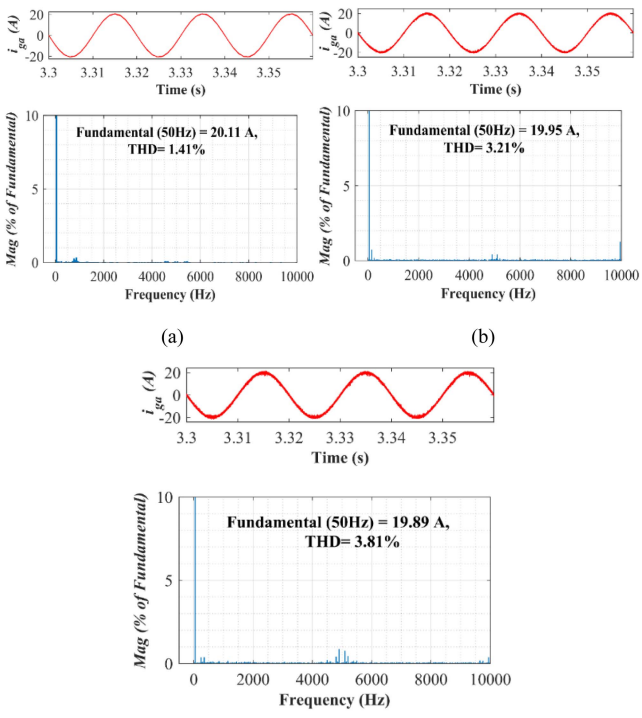

Fig. 21 Harmonic spectra with (a) WOVSSA, (b) MPSMC, and (c) LMSEF.

VI. Conclusion

This article presents operational control strategies for a grid-interactive MG tailored for remote regions with high wind energy potential. Depending on whether DFIG stator is synchronized or desynchronized with PCI, and whether PCI is synchronized or desynchronized with grid, four distinct operating states are identified. Control and performance of MG in each operating state are presented. Load flow is sustained in each operating state. Control strategy integrates an AECCF PLL to ensure fast, accurate, and smooth synchronization of DFIG stator with PCI and PCI with the grid. Nevertheless, with the proposed WOVSSA filter, GFC control enhances power quality of grid by supporting reactive power, regulating PCI voltage, and reducing harmonic distortions. Therefore, GFC enables provision of ancillary services. Cabling effects are safely neglected under lumped system model, provided there is a nearby connection to PCI for distribution systems. However, in MGs with long feeders, line impedance significantly affects current dynamics and PLL synchronization, potentially impacting control loop. Additional adaptive voltage stabilization controls are to be incorporated to nullify effect on PLL estimation loops. Fault analysis is to be considered as one possible future extension of this article. Focus of this article is to ensure reliable system performance and smooth synchronization to weak grids, despite amplitude fluctuations, while upholding power quality indices during various modes of operation.

Appendix

Control parameters and system ratings are given here.

TABLE III
System Parameters

Parameters	Values
DFIG	11 kW, 3 ph, 415 V, 50 Hz, 4 poles, $L_m = 72$ mH, $L_{si} = 1.9$ mH, $L_{ri} = 2.9$ mH, $R_s = 0.282\ \Omega$, $R_r = 0.197\ \Omega$, Stator to Rotor Turns Ratio = 1:1
BES	720 V, 21 Ah
Grid	415 V, 50 Hz
Grid SCR	R_g= 4Ω, L_g= 15 mH, SCR [24] = 2.406
Cable Impedance	R_x= 0.461 Ω, L_x= 0.08 mH
LSC Inductor	$L_{f1} = 4$ mH
BES Inverter (GFC) Inductor	$L_{f2} = 4$ mH
DC Link Capacitor	$C_{DC} = 20$ mF
AECCF Parameters	$\delta_1 = \delta_2 = \xi = 0.707$, $\delta_3 = 0.1215$, and $\omega_p = \omega_1 / \sqrt{2}$
WOVSSA Parameters	$P = 32$, $\lambda = 1.8$, and $Z = 512$ LPF cut off frequency = 100 Hz
Ripple Filters [25]	$R_f = 5\Omega$, $C_f = 5\ \mu$F

Acknowledgment

The authors would like to thank the Government of India through the Prime Minister's Research Fellowship and the ANRF for National Science Chair.

REFERENCES

[1] S. Roy and H. N. Villegas Pico, "Transient stability and active protection of power systems with grid-forming PV power plants," *IEEE Trans. Power Syst.*, vol. 38, no. 1, pp. 897–911, Jan. 2023.

[2] A. González-Cajigas, E. J. Bueno, J. Roldán-Pérez, R. Martín-López, and E. Sáiz-Marín, "Control choices to allow the parallel operation of grid-forming type-III wind turbines," *IEEE Trans. Power Electron.*, vol. 38, no. 12, pp. 15353–15364, Dec. 2023.

[3] "8% of global electricity is generated from wind," *LowerCarbonPower*, 2011. [Online]. Available: https://lowcarbonpower.org/type/wind

[4] X. Gao, Z. Xie, M. Li, S. Yang, and X. Zhang, "Analysis and mitigation of electromechanical oscillations in drivetrain for hybrid synchronization control of DFIG-based wind turbines," *IEEE Trans. Power Electron.*, vol. 39, no. 3, pp. 3002–3013, Mar. 2024.

[5] T. Wang, H. Nian, Z. Q. Zhu, H. Huang, and X. Huang, "Flexible PCC voltage unbalance compensation strategy for autonomous operation of parallel DFIGs," *IEEE Trans. Ind. Appl.*, vol. 53, no. 5, pp. 4807–4820, Sept./Oct. 2017.

[6] P. Wang, J. Ma, R. Zhang, S. Wang, T. Liu, and Y. Yang, "Stability criterion for near-area grid-forming converters under the weak grid condition," *IEEE Trans. Power Electron.*, vol. 40, no. 1, pp. 361–374, Jan. 2025.

[7] Z. Zhou, S. Pugliese, M. Langwasser, and M. Liserre, "Subsynchronous damping by battery storage system in grid-forming control," *IEEE Trans. Power Electron.*, vol. 39, no. 4, pp. 4173–4186, Apr. 2024.

[8] D. Song, Z. Zheng, J. Ren, C. Li, and Q. Xie, "SMES based reconfigured converter architecture for DFIG to enhance FRT and grid forming capability," *IEEE Trans. Appl. Supercond.*, vol. 34, no. 8, pp. 1–5, Nov. 2024.

[9] T. Dai, X. Xiao, Q. Xie, J. Ren, and Z. Zheng, "Hybrid grid-forming and grid following PMSG-SMES architecture with enhanced FRT capability," *IEEE Trans. Appl. Supercond.*, vol. 34, no. 8, pp. 1–4, Nov. 2024.

[10] A. A. Alkahtani et al., "Power quality in microgrids including supra-harmonics: Issues, standards, and mitigations," *IEEE Access*, vol. 8, pp. 127104–127122, 2020.

[11] S. K. Sahoo, S. Kumar, and B. Singh, "Wiener variable step size with variance smoothening based adaptive neurons technique for utility integrated PV-DSTATCOM system," *IEEE Trans. Ind. Electron.*, vol. 69, no. 12, pp. 13384–13393, Dec. 2022.

[12] D. Jaraniya, S. Kumar, B. Singh, and G. Modi, "Meta-heuristic optimization and variable sparsity combination of two LMS framework based charging solutions for electric transportation," *IEEE Trans. Aerosp. Electron. Syst.*, vol. 60, no. 6, pp. 8494–8503, Dec. 2024.

[13] D. Jaraniya and S. Kumar, "Power quality signal conditioning and mitigation by using LMSEXF-based control strategy for grid-tied PV assisted EV charging station," *IEEE Trans. Consum. Electron.*, vol. 70, no. 1, pp. 564–573, Feb. 2024.

[14] S. P. Singh, D. Pathak, A. Kumar, and S. Padmanaban, "An optimized fractional-order modified adaptive variable step-size LMS control approach to enhance DVR performance," *IEEE Trans. Consum. Electron.*, vol. 70, no. 1, pp. 471–483, Feb. 2024.

[15] B. Sahoo, S. R. Samantaray, and P. K. Rout, "Adaptive control scheme for hybrid microgrid resynchronization with virtual synchronous generator and active detection technique," *IEEE Trans. Ind. Appl.*, vol. 60, no. 5, pp. 7599–7612, Sept.-Oct. 2024.

[16] A. Rath, B. Pratap Behera, and B. Kumar Sethi, "Improved shunt active filter for non-ideal grid using model predictive and sliding mode control," *IEEE Trans. Consum. Electron.*, vol. 70, no. 4, pp. 6600–6608, Nov. 2024.

[17] *IEEE Application Guide for IEEE Std 1547™-2018, IEEE Standard for Interconnection and Interoperability of Distributed Energy Resources With Associated Electric Power Systems Interfaces*, IEEEStandard 1547.2-2023 (Revision IEEE Std 1547.2-2008), May 2024.

[18] Z. Zhang et al., "An adaptive enhanced complex-coefficient filter-based PLL in variable frequency grid," *IEEE Trans. Power Electron.*, vol. 39, no. 4, pp. 3950–3955, Apr. 2024.

[19] A. Boubaris, K. Dimitriadou, D. Voglitsis, N. Papanikolaou, and Y. Yang, "Active power compensation in microgrids and nanogrids under the loss of synchronization," *IEEE J. Emerg. Sel. Topics Power Electron*, vol. 12, no. 2, pp. 1456–1467, Apr. 2024.

[20] Z. Chu, G. Cui, and F. Teng, "Scheduling of software-defined microgrids for optimal frequency regulation," *IEEE Trans. Sustain. Energy*, vol. 15, no. 3, pp. 1715–1728, Jul. 2024.

[21] D. D. Edwin and M. Sucheta, "Weight optimized fixed and variable step-size adaptive filters for fetal ECG extraction," *ELSEVIER Biomed. Signal Process. Control*, vol. 98, Aug. 2024.

[22] P. I. Hubscher and J. C. M. Bermudez, "An improved statistical analysis of the least mean fourth (LMF) adaptive algorithm," *IEEE Trans. Signal Process.*, vol. 51, no. 3, pp. 664–671, Mar. 2003.

[23] G. Abad, J. López, M. Rodriguez, L. Marroyo, and G. Iwanski, "Vector control strategies for grid-connected DFIM wind turbines," *Doubly Fed Induction Mach.: Model. Control Wind Energy Gener.*, Hoboken, NJ, USA: Wiley-IEEE Press, 2011.

[24] S. Chakraborty, G. Modi, B. Singh, B. K. Panigrahi, and M.. Z. Farooqi, "A NIHOC-GI-FLL control with seasonal ToU tariff based economic power regulation for a weak grid tied optimally sized SPV-BES system," *IEEE Trans. Ind. Appl.*, vol. 61, no. 3, pp. 4414–4427, May–Jun. 2025.

[25] B. Singh, A. Chandra, and K. Al-Haddad, "Power quality problems and mitigation techniques," 2015.

Sandeep Kumar Sahoo (Member, IEEE) received the B.Tech. degree in electrical and electronics engineering from the Silicon Institute of Technology, Bhubaneswar, India, in 2014, and the MS(R) degree in energy science and engineering from the Indian Institute of Technology Guwahati, Guwahati, India, in 2017, and the Ph.D. degree from the Department of Electrical Engineering, Indian Institute of Technology Delhi, New Delhi, India, with the Power Electronics, Electrical Machines, and Drives research group in 2025.

He is currently the Deputy Manager of R&D Traction Propulsion System, Autometers Alliance Ltd., Noida, India. His research interests include microgrid, grid integration, machines and drives and power quality.

Bhim Singh (Fellow, IEEE) received the B.E. degree in electrical from the University of Roorkee, Roorkee, India, in 1977, and the M.Tech. degree in power apparatus & systems and the Ph.D. degree in power electronics, machines and drives, electrical engineering from the Indian Institute of Technology (IIT) Delhi, New Delhi, India, in 1979 and 1983, respectively.

He has been an Emeritus Professor and the ANRF National Science Chair at IIT Delhi, since July 2021. He has guided 151 Ph.D. dissertations and 184 M.E./M.Tech. /M.S.(R) theses. He has 75 granted patents and 34 filed patents. He has co-authored a textbook on power quality titled "*Power Quality Problems and Mitigation Techniques*," (John Wiley & Sons Ltd., 2015). His areas of interest include solar PV grid interface systems, microgrids, power quality monitoring and mitigation, solar PV water pumping systems, power electronics, electrical machines, drives, and electric vehicles.

Dr. Singh is the recipient of the prestigious Rashtriya Vigyan Puraskar-Vigyan Shri by the President of India for the year 2024.

Subhadip Chakraborty (Member, IEEE) received the B.Tech. degree in electrical engineering from Kalyani Government Engineering College, West Bengal, India, in 2020, and the M.Tech. degree in construction technology and management in 2022 from the Indian Institute of Technology (IIT) Delhi, New Delhi, India, where he also received the Ph.D. degree in power electronics, machines and drives, electrical engineering from the Department of Electrical Engineering, with the Power Electronics, Electrical Machines, and Drives research group in 2025.

He has been a Prime Minister's Research Fellow with the IIT Delhi. He is currently a Senior Professional with Power Grid Integration Division in Grid and Power Quality Solutions (GPQS), Hitachi Energy India Pvt. Ltd., Chennai, China. His research interests include solar and wind energy-driven three-phase three-wire and four-wire microgrids, DFIG, synchronous reluctance generators, machines and drives, grid synchronization systems, PLL/FLLs, and power quality.

Dr. Chakraborty was the recipient of the Research Excellence Award from IIT Delhi in 2025